Analytical model for light scattering of plasmonic gold nanorods with size up to 200 nm

Stuart J. Flanders,[1^] *Qiang Sun,*[2^] *Arif M. Siddiquee,*[3] *Derek Y. C. Chan,*[4,5] *and James W. M. Chon*[1*]

[1]Centre for Micro-Photonics, Dept. of Physics, Faculty of Science, Engineering and Technology, Swinburne University of Technology PO Box 218 Hawthorn 3122 Victoria, Australia

*jchon@swin.edu.au

[2]Particulate Fluids Processing Centre, Department of Chemical Engineering, University of Melbourne, Parkville 3010 VIC

[3]Australian Research Council Centre of Excellence for Advanced Molecular Imaging, Department of Chemistry and Physics, La Trobe Institute for Molecular Science (LIMS), La Trobe University, Victoria 3086, Australia

[4]Particulate Fluids Processing Centre, School of Mathematics and Statistics, University of Melbourne, Parkville 3010 VIC, Australia

[5]Department of Mathematics, Swinburne University of Technology, Hawthorn 3122, VIC, Australia

^these authors contributed equally

KEYWORDS. Gold Nanorods, Scattering, Plasmonics,

ABSTRACT

Recently, various linear and nonlinear emission processes of shape-controlled plasmonic gold nanorods have been applied in biolabelling and photothermal cancer therapy. One of the most fundamental knowledge required for understanding these processes is the field around the nanorod. Here, we present a simple analytical theoretical model for calculating near- and far-fields around prolate spheroidal (PS) and hemispherically capped cylindrical (HCC) gold nanorods beyond the quasistatic limit, for rods up to 200 nm in length ($ka \sim 1.13$, corresponding to a wavelength ~ 500 nm) and aspect ratio 5, which encompasses the parameter range of most of the biolabelling applications. We achieve this by solving the field directly from classical electrostatic model for ellipsoids, and then by introducing correction factors for different size beyond quasistatic limit and then for the shape of HCC nanorods. We validate the model with numerical simulations and correlated single particle scattering cross-section measurements using confocal laser scanning microscopy (CLSM) and transmission electron microscopy (TEM). The simple and accurate expressions will be useful in determining efficiency in any linear or nonlinear emission processes for biolabelling application that require accurate knowledge of the field around these nanorods.

Plasmonic gold nanorods have emerged as an attractive linear and nonlinear photoluminescent probes for life sciences [1-9]. Low cytotoxicity, no blinking or bleaching and high nonlinear cross-sections make them ideal biolabelling agent in the infra-red wavelength range, at which in-vivo deep tissue imaging can be achieved [10].

Wet-chemically synthesised plasmonic gold nanorods exist in various shapes but one of the most popular shape is hemispherically capped cylinders (HCCs). Recent studies demonstrated that the shape engineering of these rods can enhance the nonlinear photoluminescence performance up to 3 ~ 4 times than the blunt tipped rods [4, 5]. Theoretical efforts in trying to understand field around these shapes have mainly been based on numerical techniques such as finite element method [4], finite difference time domain method[11] , discrete dipole approximation[11], or boundary element methods[12], but at heavy cost of computational power. Simple analytical formulation for these shapes is desirable but currently only that of prolate spheroidal geometry is available[13].

Previously, Gerstan and Nitzan[14, 15] solved electric field of a molecule near a metallic spheroidal boss in a quasistatic limit for surface enhanced Raman scattering (SERS) and introduced a lightning rod factor as a universal field enhancement factor at the tip. This factor was also interpreted as the local field depolarization factors for ellipsoidal particles, which were originally introduced by Stratton[16-18] and Gans[13]. The lightning rod factor was later used by Chen et al[19], Boyd et al[20, 21], and Mohamed et al[6] to qualitatively explain second harmonic generation, two-photon luminescence, and single photon luminescence, respectively, around spheroidal geometries. However, the quasistatic solutions put severe size limitation on the nanorods being approximated, and the boundary of their validity has been rather unclear. The full electrodynamic study on the ellipsoidal particles was conducted using T-matrix method[22, 23] or by solving directly Maxwell's equations in ellipsoidal coordinate system[24, 25], but due to the complexity of the solutions, it is not widely utilised. It is therefore highly desirable to formulate a

simple analytical solution to the problem without too much restrictions on the size of the particles being studied. Fitted functions are continually developed[26] to provide corrections to the real geometries.

Here in this paper, we report an analytical fitting model that is capable of predicting field at any point on the surface of prolate spheroids and hemispherically capped cylinders with the size up to 200 nm in length ($ka \sim 1.13$, corresponding to a wavelength $\lambda = 2\pi/k \sim 500$ nm), and aspect ratio up to 5. Most of the plasmonic gold nanorods used in biolabelling and photothermal application fall within these size limits. In doing so, we calculate the field-enhancement factors responsible for enhancement in linear and nonlinear emission processes around these nanorods, such as far-field scattering, single-photon luminescence, two-photon luminescence, and SERS. We also present the new enhancement factors that can account for emission from the entire surface of these nanorods, not just at the tip.

We achieve this by firstly solving complete field expression around prolate spheroid geometry, starting from the classic expression for electric potential around an ellipsoid in quasistatic limit[16, 27] and then extending it outside of quasistatic limit by introducing size correction factors. We then extend the method to HCC nanorods and provide heuristically fitted analytical expressions for field on the surface as well as in the far-field. These expressions are validated to numerical results and to correlated single nanorod scattering cross-section measurements using confocal laser scanning microscopy (CLSM) and transmission electron microscopy (TEM). This model is simple in expression, and will be useful in determining efficiency in any linear or nonlinear emission processes that require accurate knowledge of the field around these nanorods.

THEORY OF ELECTROSTATIC FIELD AROUND PROLATE SPHEROID

Following Stratton[16] and also the details in the Supporting Information, we derived the external field of a prolate spheroidal dielectric particle, $x^2/a^2+(y^2+z^2)/c^2=1$ where $a \geq c$, with dielectric constant, ε_i in an external medium of dielectric constant, ε_e polarised by an incident constant electrostatic field $\mathbf{E}^{inc}=E_{ox}\mathbf{i}+E_{oy}\mathbf{j}+E_{oz}\mathbf{k}$ where $(\mathbf{i},\mathbf{j},\mathbf{k})$ are the unit vectors in the Cartesian system. It is most convenient to express the field in the prolate spheroid coordinate system (ξ,θ,ϕ) with the following transformation equations

$$x^2=(\xi+a^2)\cos^2\theta,\ x=\pm\sqrt{(\xi+a^2)\cos^2\theta}; \qquad (1)$$

$$y^2=(\xi+c^2)\sin^2\theta\cos^2\phi,\ y=\pm\sqrt{(\xi+c^2)\sin^2\theta\cos^2\phi}; \qquad (2)$$

$$z^2=(\xi+c^2)\sin^2\theta\sin^2\phi,\ z=\pm\sqrt{(\xi+c^2)\sin^2\theta\sin^2\phi}. \qquad (3)$$

The surface of the ellipsoid is given by $\xi = 0$, with $\xi < 0$ being the interior and $\xi > 0$ the exterior. With $h=\sqrt{a^2-c^2}$, the external field perpendicular, $E_{e\perp}(\xi,\theta,\phi)$ and parallel, $E_{e\|}$ to the surface of the ellipsoid can be expressed as (see Fig. 1)

$$E_{e\perp}(\xi,\theta,\varphi)=E_{0x}\left\{\left[1+\frac{\frac{\varepsilon_e-\varepsilon_i}{\varepsilon_e}L_1(\xi)}{1+\frac{\varepsilon_i-\varepsilon_e}{\varepsilon_e}L_1(0)}\right]\left[\frac{(c^2+\xi)\cos^2\theta}{\xi-h^2\cos^2\theta+a^2}\right]^{\frac{1}{2}}\right.$$
$$\left.-\left[\frac{\frac{\varepsilon_e-\varepsilon_i}{\varepsilon_e}ac^2}{1+\frac{\varepsilon_i-\varepsilon_e}{\varepsilon_e}L_1(0)}\right]\left[\frac{\cos^2\theta}{(c^2+\xi)(a^2+\xi)(\xi-h^2\cos^2\theta+a^2)}\right]^{\frac{1}{2}}\right\}$$
$$+(E_{0y}\cos\varphi+E_{0z}\sin\varphi)\left\{\left[1+\frac{\frac{\varepsilon_e-\varepsilon_i}{\varepsilon_e}L_2(\xi)}{1+\frac{\varepsilon_i-\varepsilon_e}{\varepsilon_e}L_2(0)}\right]\left[\frac{(a^2+\xi)\sin^2\theta}{\xi-h^2\cos^2\theta+a^2}\right]^{\frac{1}{2}}\right.$$
$$\left.-\left[\frac{\frac{\varepsilon_e-\varepsilon_i}{\varepsilon_e}ac^2}{1+\frac{\varepsilon_i-\varepsilon_e}{\varepsilon_e}L_1(0)}\right]\left[\frac{\sin^2\theta}{(c^2+\xi)^2(\xi-h^2\cos^2\theta+a^2)}\right]^{\frac{1}{2}}\right\}, \quad (4)$$

$$E_{e\parallel}(\xi,\theta,\varphi)=E_{0x}\left\{\left[1+\frac{\frac{\varepsilon_e-\varepsilon_i}{\varepsilon_e}L_1(\xi)}{1+\frac{\varepsilon_i-\varepsilon_e}{\varepsilon_e}L_1(0)}\right]\left[\frac{(a^2+\xi)\sin^2\theta}{\xi-h^2\cos^2\theta+a^2}\right]^{\frac{1}{2}}\right\} \quad (5)$$
$$+(E_{0y}\sqrt{1-\sin^2\theta\cos^2\varphi}+E_{0z}\sqrt{1-\sin^2\theta\sin^2\varphi})\left\{\left[1+\frac{\frac{\varepsilon_e-\varepsilon_i}{\varepsilon_e}L_2(\xi)}{1+\frac{\varepsilon_i-\varepsilon_e}{\varepsilon_e}L_2(0)}\right]\left[\frac{(c^2+\xi)}{\xi-h^2\cos^2\theta+a^2}\right]^{\frac{1}{2}}\right\}$$

A full derivation of these expressions can be found in the Supporting Information. Eqs. 4 and 5 express the field at any point in the space, either on the rod or away from the rod, which can be calculated from any arbitrary incident constant field $\mathbf{E}^{\text{inc}}$. The factors $L_1(\xi)$, $L_2(\xi)$, and $L_1(0)$, $L_2(0)$ are given by

$$L_1(\xi)=ac^2\left(-\frac{1}{2h^2\sqrt{a^2+\xi}}-\frac{1}{2h^3}\ln\left|\frac{\sqrt{a^2+\xi}+h}{\sqrt{a^2+\xi}-h}\right|\right), \quad (6)$$

$$L_2(\xi)=ac^2\left(\frac{\sqrt{a^2+\xi}}{2h^2(c^2+\xi)}-\frac{1}{4h^3}\ln\left|\frac{\sqrt{a^2+\xi}+h}{\sqrt{a^2+\xi}-h}\right|\right), \quad (7)$$

$$L_1 = L_1(0) = ac^2\left(-\frac{1}{h^2 a} - \frac{1}{2h^3}\ln\left|\frac{a+h}{a-h}\right|\right), \tag{8}$$

$$L_2 = L_2(0) = ac^2\left(\frac{a}{2h^2c^2} - \frac{1}{4h^3}\ln\left|\frac{a+h}{a-h}\right|\right). \tag{9}$$

As it is always possible to set $|\mathbf{E}^{inc}| = 1$ without loss of generality, we define the field enhancement factor $\mathcal{L}(\xi,\theta,\varphi)$ at any point around a prolate spheroid by

$$\mathcal{L}(\xi,\theta,\varphi) = \sqrt{\left|E_{e\perp}\right|^2 + \left|E_{e\parallel}\right|^2}, \tag{10}$$

and the integrated field enhancement factor $\mathcal{L}_s$ over the entire surface of a nanorod is

$$\mathcal{L}_S = \frac{\iint_S \mathcal{L}(\xi,\theta,\varphi)dS}{Surface\ Area}. \tag{11}$$

The quantity $\mathcal{L}_S$ in Eq. 11 can be used to gauge the signal enhancement in SERS, single- or two-photon luminescence enhancement. Far-field scattering cross section can be calculated by

$$\sigma_{sca} = \frac{k^4}{6\pi}|\alpha|^2, \tag{12}$$

where $k = 2\pi/\lambda$, and α is the polarizability of the particle, given by

$$\alpha_{1,2} = 4\pi a c^2 \frac{\varepsilon_e - \varepsilon_i}{3\varepsilon_i + 3L_{1,2}(\varepsilon_e - \varepsilon_i)}. \quad (13)$$

SIZE AND DAMPING CORRECTIONS TO THE ELECTROSTATIC MODEL

It is clear that as the size of particle becomes comparable or larger than the wavelength these expressions are no longer valid and electrodynamic calculations are needed to account the variations in the incident field over the size of the particle and associated scattering. As the size increases, phase-retardation effects red-shift the surface plasmon resonance position and the radiation damping broadens the peak. In order to account for both of these deviations around $ka \sim 1$, we use the following expression to account for damping in the L factor,

$$L^{damp} = L\left[1 - D(a) - i\Gamma(V)\right]. \quad (14)$$

Here L is the electrostatic depolarization factor in Eqs. 8-9, $D(a)$ is the retardation correction and $\Gamma(V)$ is a radiation damping correction up to 3rd order. In comparison to previous attempts, this expression effectively decouples the two effects and corrects with high order terms. The explicit expressions for the correction factors are

$$D(a) = \sum_{j=0}^{3} b_j \left(\frac{a\sqrt{\varepsilon_e}}{\lambda}\right)^j, \quad (15)$$

and

$$\Gamma(V) = \sum_{j=1}^{2} c_j \left(\frac{4\pi^2 V}{3\lambda^3} (\varepsilon_e - \varepsilon_i)^{\frac{3}{2}} \right)^j , \tag{16}$$

where b_j and c_j are fitting coefficients, and a is longitudinal length and V is volume of the rod.

SHAPE CORRECTION TO THE ELECTROSTATIC MODEL

The above correction expressions for L^{damp} can be extended to other shapes such as HCC nanorods, which are the most common form of gold nanorods produced by wet-chemical synthesis[28, 29]. The light scattering properties of these nanorods are often approximated by the electrostatic model for prolate spheroidal nanorods[30], but these approximations do not give accurate peak positions and scattering strengths[26]. Attempts were made to account the inaccuracies in ensemble spectra, by correcting depolarization L factors in the polarizability of the nanorod. However, applying this factor in Eqs. 10-12 had limited success in correcting near-field and far-field scattering strengths. In order to accurately account for these deficiencies, Eq. 10 is multiplied by an angular correction function $f(\theta, AR)$. This correction function is a heuristically fitted function, which can be found by numerical simulation result for HCC nanorod at quasistatic limit (i.e., $ka < 0.04$). For HCC we found

$$f(\theta, AR) = \frac{1}{\alpha_0 + \alpha_1 \cos \beta_1 \theta (\mathrm{e}^{-(\gamma_1 \theta)^2} + \mathrm{e}^{-(\gamma_2 \theta)^2})} , \tag{17}$$

with the fitted coefficients: $\alpha_0 = 0.91$, $\alpha_1 = 0.31\ AR - 0.06$, $\beta_1 = 2.24\ AR - 2.11$, $\gamma_1 = 1.62\ AR - 1.84$, and $\gamma_2 = 6.70\ AR - 11.72$ (AR is aspect ratio of rod). Note that this function is unique to HCC shape only

and other shapes such as bipyramids or dumbbells require new fitting expressions. The size and damping effect can be applied by using Eq. 14-16 in the same manner as prolate spheroids.

COMPARISON WITH NUMERICAL SIMULATION

In order to test the range of validity of the electrostatic expressions in Eqs. 4-5 (henceforth referred to as ES model) at $ka > 0$ for the electric field around a prolate spheroidal gold nanorod subjected to an oscillating field, we show a comparison between the ES model and a numerical FEM simulation (COMSOL Multiphysics). In the simulation, we used gold nanorods of fixed aspect ratios of 2.5, 3.5 and 4.5, but varied the dimensions of the rods in vacuum ($\varepsilon_e = 1$). We used dielectric function of gold from Rakic et al.[31] for the nanorods.

In Fig. 2, the field enhancement factor at the entire surface $\mathcal{L}_S$, and far-field scattering cross sections

σ_{sca} are shown at different volumes using the ES model (black dotted line) and numerically simulated electrodynamic model (red lines). One can see that only for smaller rods the ES model matches with the numerical simulations, with significant quantitative deviations from the ES model for the larger rod. For prolate ellipsoids at an aspect ratio (AR) of 2.5, deviations are evident at ka as small as 0.08 ($a \sim 15$ nm) (Fig. 2a), which is in line with the previous observations by Barber et al[22, 23], where the deviation of electrodynamic model from electrostatic model started at $a/\lambda \sim 0.02$. As the nanorod size increases, the deviation involves strong red-shift in resonance position, as well as initial increase in enhancement with the volume increase followed by a decrease with further increase in volume. Far-field results (Fig. 2b) are also similar to the field enhancement results in Fig. 2a.

Interestingly, for *ka* between 0.08 ~ 0.2 there is an *increase* in the enhancement before the decrease. This increase is partly due to the red-shift of the resonance associated with phase retardation. Barber et al [22, 23] previously observed this increase, but was ignored in their first order correction to the radiation damping. However, it can be seen from other aspect ratio plots that such increase is only prominent in short aspect ratio rods. Fig. 2c, d show the result for AR = 3.5 and Figs. 2e, f for AR = 4.5. All of them show minimal initial increase in field enhancement and more radiative damping takes over. The damping effect is characterised by the decrease in enhancement strength, broadening of the peak and the red-shift.

The radiative damping is caused by increase in radiation from dipole resonance of plasmon, which scales with the number of electrons in the rods. First order correction to this damping was discussed by both Wokaun et al[18] and Barber et al[23], who added an imaginary term proportional to the volume of the rod in the *L* factors. This was later amended by Boyd et al[20] to account for the dielectric function of the surrounding medium. Based on this framework, both Sonnichsen et al [32], Novo et al [33] experimentally accounted for the radiative damping with respect to the width of the resonance, but did not fully account for the magnitude of the field enhancement or the cross sections. Again the damping term was the first order correction to the volume and applied to small population of the hemispherically-capped cylindrical nanorods.

Fig. 3 shows the results by the corrected ES model (blue dotted line) in Eqs. 10 - 11 with 3rd order damping correction for L_1^{damp} using Eqs. 14-16. This model accurately predicts the redshift, the increase in magnitude followed by decrease and broadening of the resonance as seen in comparison with FEM results. This is valid up to half lengths of 80 nm, which is equivalent to *ka* ~ 0.72 at the resonance peak, and up to *ka* ~ 1.13 in the blue side of the resonance. We have repeated the correction for the other aspect ratio of the rods, and the damping coefficients b_j and c_j in Eqs. 31 and 32 are tabulated in the Table 1. Other aspect ratio results (AR = 3.5 and 4.5) are shown in Fig. 3, which show very good agreement.

APPLICATION TO HEMISPHERICALLY CAPPED CYLINDRICAL NANORODS

With the successful account of large prolate spheroidal nanorods with the corrected ES model, it can be extended to other shapes such as HCC nanorods.

Using the correction function Eq. 17, field magnitude on various nanorod surfaces with respect to the radial angle θ at quasistatic limit is plotted for selected aspect ratios (Fig. 4). The plots show good agreement between the corrected field and numerically simulated field (FEM) for HCC surface.

Based on this corrected quasistatic **E** field at the surface of HCC, the total surface enhancement factor $\mathcal{L}_s$ can now be calculated by surface integration. Again, in order to correct for the size up to $ka \sim 1.13$,

correction coefficients for $D(a)$ and $\Gamma(a)$ are determined by the comparison with numerical simulation. The resulting spectra are shown in Fig. 5 together with the numerical simulation results. Far-field scattering are also shown, which all demonstrate good agreements. In comparison to prolate spheroids, the HCC shows slightly more red-shifted SPR peaks but the trend is generally similar. Larger rods have red-shifted and broader peaks than at quasistatic limit.

EXPERIMENTAL VALIDATION

In order to validate the model, we measured far-field scattering cross sections (σ_{sca}) of single HCC gold nanorods by confocally detecting back scattered photons using a home-built laser confocal scanning microscopy (CLSM) setup.

We also performed correlated optical and transmission electron microscopy (TEM) on the same particles. This brings accurate morphological information about nanoparticles shape and size, and allows us to investigate size effect on σ_{sca} at single particle level. We used TEM coordinated grid on substrate which allows us to identify the same areas in optical and electron microscopes.

Gold nanorods with HCC shape were purchased from Nanoseedz. The TEM analysis of 30 individual nanorods showed that the nanorods are mostly HCC in shape, with average width 25.5 ± 3.7 nm, length 78.6 ± 8.0 nm, and aspect ratio 3.2 ± 0.4.

Fig. 6 shows the measured peak scattering cross-sections of nanorods with respect to their aspect ratio. Overlaid lines are the analytical model (corrected ES for HCC) lines for an average length and variation in width. 67% of experimental points lies within the standard deviation of volume (dashed green lines), showing good agreement.

In summary, we have presented a simple analytical model for calculating near- and far-field strengths around prolate spheroidal and HCC gold nanorods beyond the quasistatic limit, up to 200 nm in length (ka ~ 1.13, corresponding to a wavelength ~ 500 nm) and aspect ratio 5, which are generally the size limits of most of the biolabelling and photothermal application. We achieved this by solving the field

explicitly from quasistatic model for ellipsoids, and then by introducing correction factors for other shapes (HCC) and size. We validated the theory with numerical simulations and correlated single particle scattering cross-section measurements using confocal laser scanning microscopy (CLSM) and transmission electron microscopy (TEM). The corrected ES model is easy to use, accurately calculates near-fields around nanorods and far-field scattering. It also can be easily extended to other cylindrically symmetric shapes, such as bipyramids, or dumbbells. It will be extremely useful in determining efficiency in any linear or nonlinear emission processes for biolabelling application that require accurate knowledge of the field around these nanorods.

ACKNOWLEDGMENT

J. W. M. C. would like to thank the Australian Research Council for the funding of the research, with funding ID FT110101038 and DP110102870. Q. S. was supported by the Australian Research Council through a Discovery Early Career Researcher Award (DE150100169). D. C. was supported in part by an Australian Research Council Discovery Project Grant DP170100376.

METHODS

Gold nanorods with HCC shape were purchased from Nanoseedz and London finder (LF400 Cu mesh) TEM grids were used for electron microscopy. TEM grids were taped on the top of glass substrates, and then the nanorods were mixed with 1% PVA solution and then spin coated on the top of the TEM grids for single particle measurements. The TEM analysis of 30 individual nanorods showed that the nanorods are mostly HCC in shape, with average width 25.5 ± 3.7 nm, length 78.6 ± 8.0 nm, and aspect ratio 3.2 ± 0.4.

Single particle scattering measurements were performed on our homebuilt CLSM setup. We used circularly polarized laser beam (Tsunami, Spectra-Physics) to excite longitudinal plasmon mode of the nanoparticles. We sequentially recorded scattering images of the same particles for a range of wavelengths between 700 nm to 900 nm in 10 nm increments which allows for the wavelength dependent excitation response for a number of single nanoparticles to be determined simultaneously, and ensures the scattering intensity is measured at the peak LSPR wavelength (λ_{LSPR}) for each particle. Each spectrum at different excitation wavelength was continuously monitored by a spectrometer (Ocean Optics). The laser beam was then focused onto the sample through a 1.4 NA oil immersion objective. Sample was mounted on a computer controlled 3D high resolution scanning stage (Physik Instrument stage, 200μm × 200μm × 200μm). Same objective was used to collect the back scattered signal. Then σ_{sca} of individual particles were measured from these confocally detected back-scattered photons using a photomultiplier tube (PMT, Oriel). The scattering intensity of individual particle was obtained by integrating the photomultiplier tube voltage over the individual spots. The number of scattered photons collected per unit time (F_{sca}) can be expressed as

$$F_{sca} = \frac{1}{2}\sigma_{sca}\varphi_{sca}I, \tag{27}$$

where φ_{sca} is the collection efficiency of the setup, I is the incident photon flux (in photons/s/cm^2), and σ_{sca} is the scattering cross-section (in m^2). The factor (1/2) is used because of the circular polarization of the excitation beam. More details of the experiment can be found elsewhere[34]. The measured cross sections are corrected for the carbon grid substrate damping based on FEM simulations. TEM carbon grid is made up of thin (4 ~ 5 nm) carbon film, which causes significant reduction in plasmon resonance[35, 36]. We have corrected the cross-sections by simulating the damping using FEM for individual size and

shape of the HCC nanorods. Up to 80% reduction in scattering strength, depending on the aspect ratio and peak SPR wavelength, was observed, which were accounted for in the final values.

FIGURES

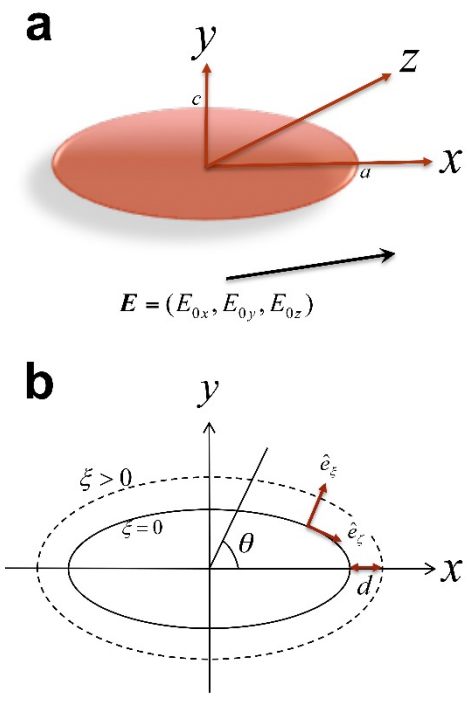

Fig. 1 Sketch of the geometry and coordinate system of a prolate spheroid. (a) Cartesian coordinate system on the prolate spheroid with longitudinal length a and transverse length c. Field $\mathbf{E}^{inc} = (E_{0x}, E_{0y}, E_{0z})$ is the arbitrary incident field. (b) x-y plane projection of the prolate spheroid. Vectors $\hat{e}_\xi$, $\hat{e}_\zeta$, $\hat{e}_\eta$ are the unit vectors that are perpendicular to the surface, parallel to the surface in x-y plane, and parallel to the surface in y-z plane, respectively. Angle θ is shown, also with spheroid surface given by $\xi = 0$.

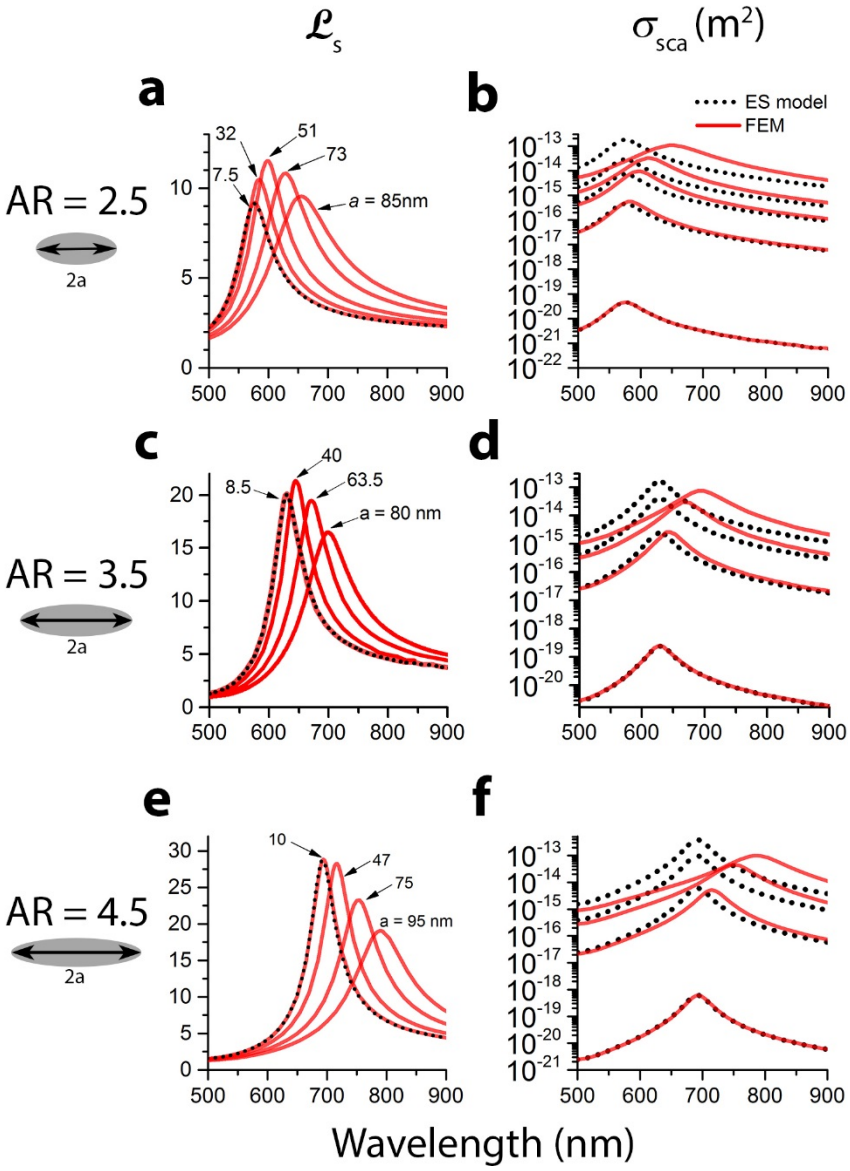

Fig. 2 (a) Surface integrated field enhancement factor $\angle_s$ given by Eq. 11 for aspect ratio 2.5 prolate spheroidal gold nanorods (black dotted line). Numerically simulated electrodynamic field enhancement using FEM (red lines). (b) Far-field scattering cross sections (σ_{sca}) calculated using Eq. 12 are shown for aspect ratio 2.5 prolate spheroidal gold nanorods. (c) $\angle_s$, (d) σ_{sca} plots for aspect ratio 3.5 rods, (e), $\angle_s$, (f) σ_{sca} for aspect ratio 4.5 rods. Half length of the rod *a* are specified in the figures. The ES model is only accurate for $ka < 0.08$.

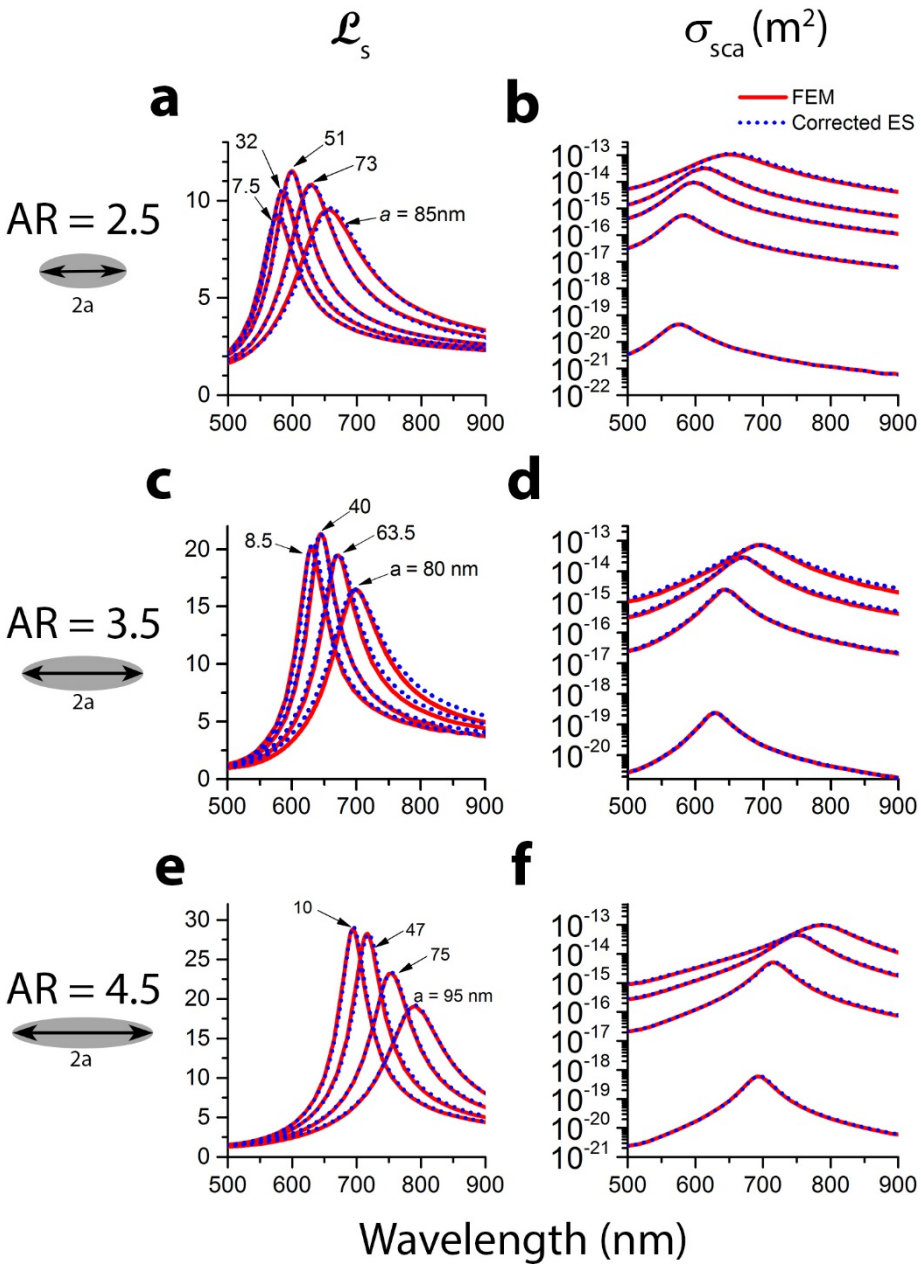

Fig. 3 (a) Surface integrated field enhancement factor $\mathcal{L}_s$ for aspect ratio 2.5 prolate spheroidal gold nanorods. Calculated with damping corrected ES model for prolate spheroids (Eq. 11, 14-16, blue dotted lines), and compared with numerically simulated electrodynamic field enhancement using FEM (red lines). (b) Damping corrected far-field scattering cross sections (σ_{sca}) calculated using Eqs. 12, 14-16

are for the same rods in (a). (c) $\angle_s$, (d) σ_{sca} plots for aspect ratio 3.5 rods, (e), $\angle_s$, (f) σ_{sca} for aspect ratio 4.5 rods. Half length of the rod *a* are specified in the figures. Note that the corrected ES model matches perfectly the electrodynamic simulation up to *ka* ~ 1.13.

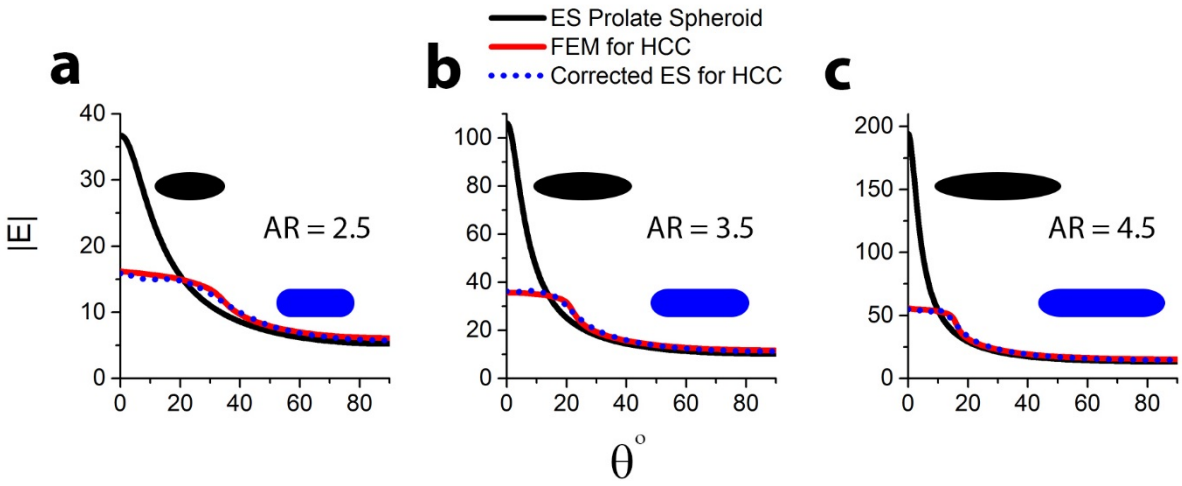

Fig. 4 Comparison of surface fields for prolate spheroid calculated using ES model (Eqs. 10, black line) and corrected ES model (Eq. 10, 14-16 for HCC, blue line) for aspect ratio 2.5, 3.5, and 4.5. Overlaid is the FEM result for HCC (red line) showing good agreement between the corrected ES model and the numerical simulation results.

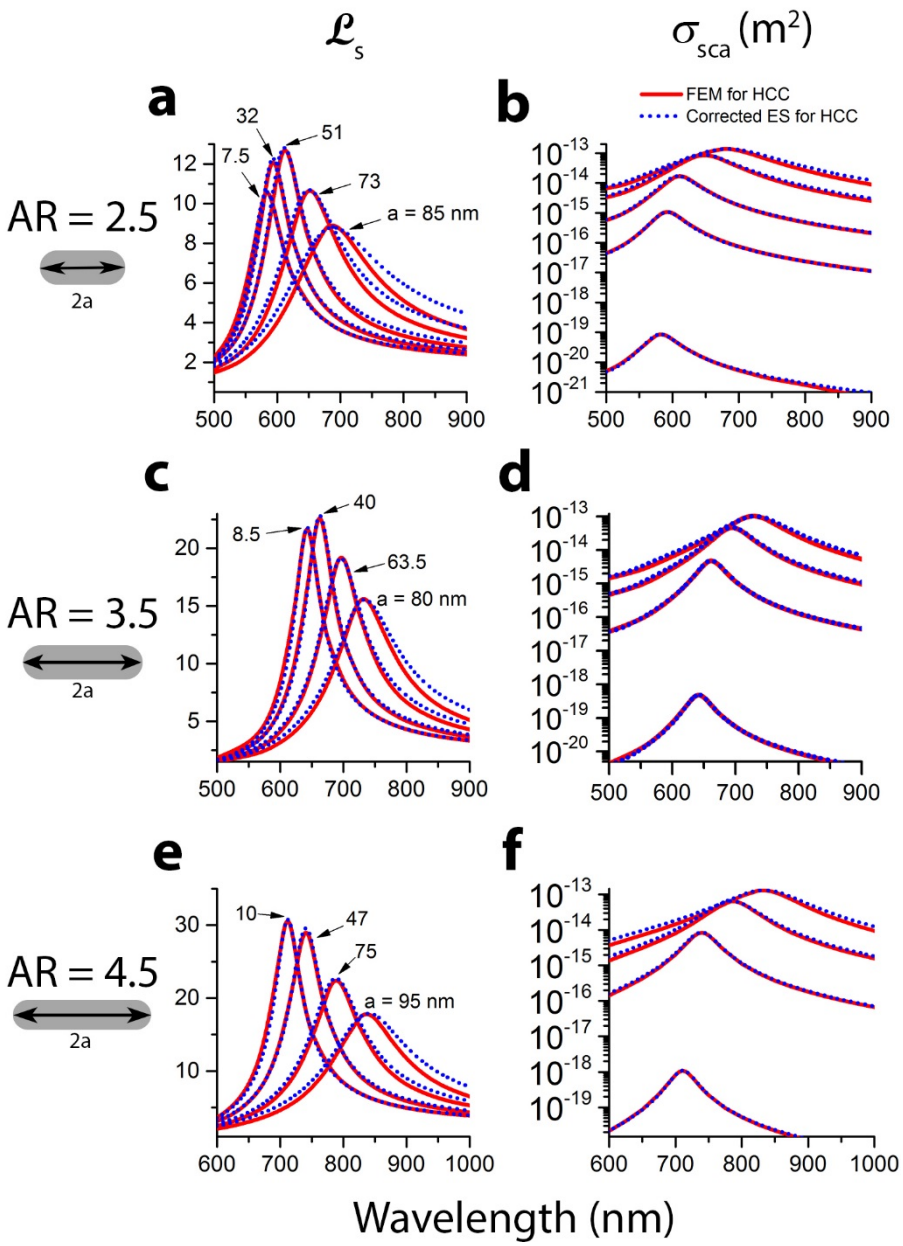

Fig. 5 (a) Surface integrated field enhancement factor $\mathcal{L}_s$ for aspect ratio 2.5 HCC gold nanorods. Calculated with damping corrected ES model for HCCs (Eq. 11, 14-17, blue dotted lines), and compared with numerically simulated electrodynamic field enhancement using FEM (red lines). (b) Damping corrected far-field scattering cross sections calculated using Eqs. 12, 14-17 are shown for the same rods

in (a). (c) $\angle_s$, (d) σ_{sca} plots for aspect ratio 3.5 HCC rods, (e), $\angle_s$, (f) σ_{sca} for aspect ratio 4.5 HCC

rods. Half length of the rod *a* are specified in the figures. Note that the corrected ES model for HCC shows good agreement with electrodynamic simulation up to *ka* ~ 1.13.

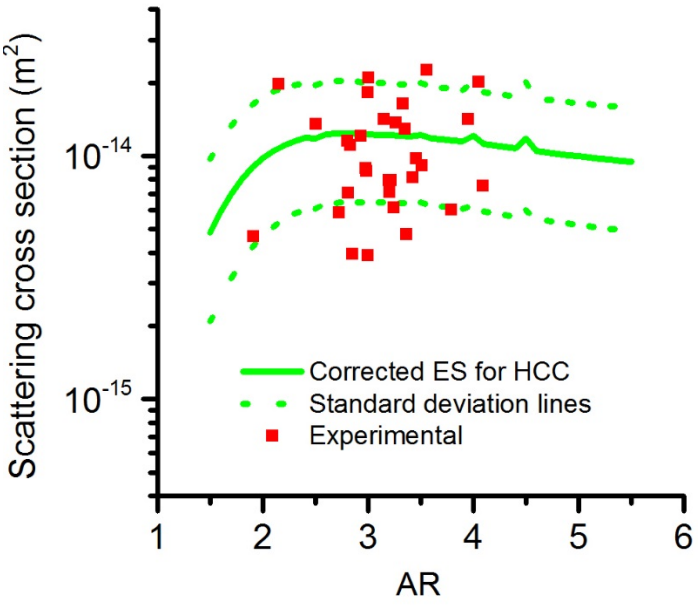

Fig. 6 Experimental scattering cross-section measurements of single HCC nanorods (red squares) overlaid with corrected ES model for HCC (green solid line). The corrected ES model line was calculated based on the average HCC nanorod size (25 nm width, 78 nm length). The green dashed lines are the theoretical cross sections at standard deviation of the volumes.

	$D(a)$				$\Gamma(V)$	
	b_0	b_1	b_2	b_3	c_1	c_2
Prolate Spheroids	0	0.2 ± 0.0	17.5 ± 0.5	25 ± 0.0	27 ± 3.0	-0.15 ± 0.0
HCCs	-0.07 ± 0.00	0.1 ± 0.0	23.4 ± 0.7	20 ± 0.0	0.26 ± 0.05	-0.18 ± 0.04

Table 1. Coefficients used in ES model damping correction functions (Eqs. 14-16) for prolate spheroids (Fig. 3 plots) and HCCs (Fig. 5 plots).

REFERENCES

1. Wang, H.; Huff, T. B.; Zweifel, D. A.; He, W.; Low, P. S.; Wei, A.; Cheng, J. X. *Proceedings of the National Academy of Sciences of the United States of America* **2005,** 102, (44), 15752-15756.
2. Durr, N. J.; Larson, T.; Smith, D. K.; Korgel, B. A.; Sokolov, K.; Ben-Yakar, A. *Nano Letters* **2007,** 7, (4), 941-945.
3. Wang, T. Y.; Halaney, D.; Ho, D.; Feldman, M.; Milner, T. *Lasers in Surgery and Medicine* **2013,** 45, 50-50.
4. Siddiquee, A. M.; Taylor, A. B.; Syed, S.; Lim, G. H.; Lim, B.; Chon, J. W. M. *Journal of Physical Chemistry C* **2015,** 119, (51), 28536-28543.
5. Gao, N. Y.; Chen, Y.; Li, L.; Guan, Z. P.; Zhao, T. T.; Zhou, N.; Yuan, P. Y.; Yao, S. Q.; Xu, Q. H. *Journal of Physical Chemistry C* **2014,** 118, (25), 13904-13911.
6. Mohamed, M. B.; Volkov, V.; Link, S.; El-Sayed, M. A. *Chemical Physics Letters* **2000,** 317, (6), 517-523.
7. Bouhelier, A.; Bachelot, R.; Lerondel, G.; Kostcheev, S.; Royer, P.; Wiederrecht, G. P. *Physical Review Letters* **2005,** 95, (26), 267405.
8. Yorulmaz, M.; Khatua, S.; Zijlstra, P.; Gaiduk, A.; Orrit, M. *Nano Letters* **2012,** 12, (8), 4385-4391.
9. Rao, W. Y.; Li, Q.; Wang, Y. Z.; Li, T.; Wu, L. J. *Acs Nano* **2015,** 9, (3), 2783-2791.
10. Horton, N. G.; Wang, K.; Kobat, D.; Clark, C. G.; Wise, F. W.; Schaffer, C. B.; Xu, C. *Nature Photonics* **2013,** 7, (3), 205-209.
11. Liu, M. Z.; Guyot-Sionnest, P.; Lee, T. W.; Gray, S. K. *Physical Review B* **2007,** 76, (23).
12. Funston, A. M.; Novo, C.; Davis, T. J.; Mulvaney, P. *Nano Letters* **2009,** 9, (4), 1651-1658.
13. Gans, R. *Ann. Phys.* **1912,** 37, (5), 881-900.
14. Gersten, J.; Nitzan, A. *Journal of Chemical Physics* **1980,** 73, (7), 3023-3037.
15. Gersten, J.; Nitzan, A. *Journal of Chemical Physics* **1981,** 75, (3), 1139-1152.
16. Stratton, J. A., *Electromagnetic Theory*. McGraw-Hill: New York and London, 1941.
17. Liao, P. F.; Wokaun, A. *Journal of Chemical Physics* **1982,** 76, (1), 751-752.
18. Wokaun, A.; Gordon, J. P.; Liao, P. F. *Physical Review Letters* **1982,** 48, (14), 957-960.
19. Chen, C. K.; Heinz, T. F.; Ricard, D.; Shen, Y. R. *Physical Review B* **1983,** 27, (4), 1965-1979.
20. Boyd, G. T.; Rasing, T.; Leite, J. R. R.; Shen, Y. R. *Physical Review B* **1984,** 30, (2), 519-526.
21. Boyd, G. T.; Yu, Z. H.; Shen, Y. R. *Physical Review B* **1986,** 33, (12), 7923-7936.
22. Barber, P. W.; Chang, R. K.; Massoudi, H. *Physical Review B* **1983,** 27, (12), 7251-7261.
23. Barber, P. W.; Chang, R. K.; Massoudi, H. *Physical Review Letters* **1983,** 50, (13), 997-1000.
24. Asano, S.; Yamamoto, G. *Applied Optics* **1975,** 14, (1), 29-49.
25. Calander, N.; Willander, M. *Journal of Applied Physics* **2002,** 92, (9), 4878-4884.
26. Prescott, S. W.; Mulvaney, P. *Journal of Applied Physics* **2006,** 99, (12), 123504.
27. Kusne, A. G.; Lambeth, D. N. *Ieee Transactions on Electron Devices* **2010,** 57, (3), 712-719.
28. Yu, Y. Y.; Chang, S. S.; Lee, C. L.; Wang, C. R. C. *Journal of Physical Chemistry B* **1997,** 101, (34), 6661-6664.
29. Perez-Juste, J.; Liz-Marzan, L. M.; Carnie, S.; Chan, D. Y. C.; Mulvaney, P. *Advanced Functional Materials* **2004,** 14, (6), 571-579.
30. Brioude, A.; Jiang, X. C.; Pileni, M. P. *Journal of Physical Chemistry B* **2005,** 109, (27), 13138-13142.
31. Rakic, A. D.; Djurisic, A. B.; Elazar, J. M.; Majewski, M. L. *Applied Optics* **1998,** 37, (22), 5271-5283.

32. Sönnichsen, C.; Franzl, T.; Wilk, T.; Von Plessen, G.; Feldmann, J.; Wilson, O.; Mulvaney, P. *Physical Review Letters* **2002,** 88, (7), 774021-774024.
33. Novo, C.; Gomez, D.; Perez-Juste, J.; Zhang, Z.; Petrova, H.; Reismann, M.; Mulvaney, P.; Hartland, G. V. *Physical Chemistry Chemical Physics* **2006,** 8, (30), 3540-3546.
34. Taylor, A. B.; Siddiquee, A. M.; Chon, J. W. M. *Acs Nano* **2014,** 8, (12), 12071-12079.
35. Habteyes, T. G.; Dhuey, S.; Wood, E.; Gargas, D.; Cabrini, S.; Schuck, P. J.; Alivisatos, A. P.; Leone, S. R. *Acs Nano* **2012,** 6, (6), 5702-5709.
36. Hobbs, R. G.; Yang, Y.; Fallahi, A.; Keathley, P. D.; De Leo, E.; Kartner, F. X.; Graves, W. S.; Berggren, K. K. *Acs Nano* **2014,** 8, (11), 11474-11482.